Geomorphology 372 (2021) 107469

Contents lists available at ScienceDirect

Geomorphology

journal homepage: www.elsevier.com/locate/geomorph

Rapid flood intensification and environmental response of the Lower Meuse during the Allerød-Younger Dryas climate transition

Fei Peng [a,*], Ronald van Balen [a,b], Christiaan Beets [a], Cornelis Kasse [a], Maarten Prins [a], Nathalie Van der Putten [a], Simon Troelstra [a], Hessel Woolderink [a], John Van der Woude [a]

[a] Department of Earth Sciences, Vrije Universiteit Amsterdam, De Boelelaan 1085, 1081 HV Amsterdam, the Netherlands
[b] TNO - Geological Survey of the Netherlands, Princetonlaan 6, 3584 CB Utrecht, the Netherlands

ARTICLE INFO

Article history:
Received 7 April 2020
Received in revised form 5 September 2020
Accepted 6 October 2020
Available online 9 October 2020

Keywords:
Grain-size distribution
End-member modelling
Lateglacial
Lower Meuse flood

ABSTRACT

Lateglacial climatic oscillations exerted profound impacts on the Meuse fluvial system. In the Lower Meuse (southern Netherlands), geomorphological studies in the last decades mainly centred on Lateglacial vegetation evolution, channel pattern changes and river terrace formation. Little information has been reported about the paleohydrology and its relation with the regional climate conditions. This study investigates a sediment core that contains flood sediments deposited from the early Allerød up to the middle Holocene. We conducted grain size analysis, thermogravimetric analysis (organic matter and calcium carbonate content), pollen and macrofossil analysis, and determined the oxygen and carbon stable isotope ratios of biogenic carbonate (opercula of the freshwater gastropod *Bithynia tentaculata*). The chronology of the core is based on AMS ^{14}C dating and pollen biostratigraphical correlation. The pollen and macrofossil studies reveal that the core site was a lake environment during the Allerød and Younger Dryas periods. The oxygen isotope record in conjunction with organic matter and carbonate content are believed to have captured the intra-Allerød Cold Period (IACP). The synchronous variation of oxygen and carbon isotopes with calcium carbonate content indicates a dominant evaporation effect on carbonate chemistry of the lake environments during the warm Allerød interstadial. End-member modelling decomposes the grain-size distributions into two sandy end members (bed load) and two silty-clayey end members (suspended load). In order to highlight the flood signal, we constructed two flood energy indexes (FEI-1 and FEI-2) that reflect the coarseness of the suspended load and bed load, respectively. Both indexes show a relatively high flood condition during the IACP, followed by a low flood phase in the Late Allerød and quickly intensified flood conditions at the onset of the Younger Dryas. In the second phase of the Younger Dryas, deposition of sandy aeolian sediments to the core site complicates the paleoflood identification using FEI-2 (bed load). This study shows a high sensitivity of the hydrological process and sedimentary environment at the Lower Meuse to the regional climate system.

1. Introduction

The Lateglacial is characterized by a series of large and abrupt climate shifts which are expressed by warming and cooling alternations. During the transition from Greenland Interstadial-1 (Bølling-Allerød) to Greenland Stadial-1 (Younger Dryas) occurring at ~12.9 ka Cal BP (e.g., Rasmussen et al., 2006; Clark et al., 2012; Rasmussen et al., 2014), climatic oscillations have induced important impacts on the global ecological environment and hydrological processes. Therefore, the Lateglacial period is suitable to study the effects of rapid climatic changes on paleohydrological processes.

In the southern Netherlands, the Meuse river experienced a series of river morphological changes from the Lateglacial to the Holocene (Vandenberghe et al., 1994; Kasse et al., 1995; Tebbens et al., 1999; Woolderink et al., 2018). The general consensus is that the river changed from a multi-channel low-sinuosity system in the Bølling to a high-sinuous pattern during the Allerød, and this was followed by a braided river system in the Younger Dryas cold period. From the Holocene onwards, the Meuse became a single-channel with a meandering style again.

For the Holocene time period, Peng et al. (2019), Peng et al. (2020) and Toonen et al. (2015) respectively reconstructed paleofloods for the Lower Meuse and Lower Rhine by analyzing fluvial sediments preserved in various sedimentological settings (levee, floodplain, channel-fills). However, the highly variable Lateglacial fluvial network makes it challenging to find suitable sediment records which allow the study of the flooding stages in the Lateglacial period, and this further hinders the correlation of the flooding regime with climatic oscillations. This is because the Allerød fluvial terrace has largely been eroded by the

* Corresponding author.
E-mail address: fpeng89@163.com (F. Peng).

https://doi.org/10.1016/j.geomorph.2020.107469

wide, braided system in the Younger Dryas, and to a minor extent also by the Holocene Meuse river. To further extend the paleoflooding history to the Lateglacial and to understand its sensitivity to rapid climate change, we analyzed a sediment core from a small fluvial lake which formed as a result of channel neck cut-off during the early Allerød (Van Leeuwen, 2014). Multiple proxy-analyses were applied, including grain size, organic matter and calcium carbonate content, pollen, macro fossils and oxygen and carbon isotopes from biogenic carbonate. End-member modelling analysis was applied to decompose the grain-size dataset into a certain number of representative components reflecting suspended loads and bed loads. The record was chronologically constrained through AMS ^{14}C dating and pollen-based biostratigraphical correlation. Below, we first show the lithological characteristics and grain size results, followed by local pollen and macro fossil zone subdivision. Second, we discuss the Lateglacial vegetation history in the Lower Meuse catchment, supported by our new pollen data. In addition, the local pollen zone subdivision is correlated to the regional established pollen assemblage zones (Hoek, 1997) to obtain the biostratigraphical information. Then, we study the Lateglacial paleofloods of the Lower Meuse, using the grain-size end-member modelling method, assisted by other analyzed sedimentary parameters. Finally, we study the linkage of the flooding conditions and sedimentological processes with the regional and local climate changes.

2. Research area

2.1. Geomorphological setting

The ~925 km long Meuse river has a catchment covering 33,000 km^2, and flows through north-eastern France, Belgium and the southern part of the Netherlands (Fig. 1A). In Nijmegen, it turns to the west before flowing into the North Sea (Fig. 1A). The Lower Meuse valley (LMV) is the part situated between Maastricht and Nijmegen. In the LMV the Meuse flows through the Roer Valley Rift System, which consists of Roer Valley Graben, Peel Block and Venlo Block (Fig. 1A). These three blocks are separated by the NW-SE oriented fault zones (Fig. 1A). The Roer Valley Graben experiences most subsidence and has Quaternary deposits with a thickness >200 m (De Mulder et al., 2003). The Peel Block has been strongly uplifted, whereas the Venlo Block takes an intermediate position: rising compared to the Roer Valley Graben but subsiding as compared to the Peel Block (Hoek et al., 2017). The tectonic activity is reflected in the present Meuse morphology in the LMV. In the Roer Valley Graben, the Meuse valley is characterized by a broad Holocene floodplain (width: ~3.5 km) and a high meandering channel (Fig. 1B). On the Peel Block, the Holocene floodplain is very narrow (~500 m wide) along a relatively straight and incised channel (Fig. 1B). On the Venlo Block, the river channel exhibits a low-sinuosity course and the Holocene floodplain gradually widens towards the Rhine–Meuse delta. This study focuses on the LMV on the Venlo Block (Fig. 1B, C), where terraces reflect stepwise incision and changing fluvial patterns from the Lateglacial to early Holocene (Kasse et al., 1995; Woolderink et al., 2018) (Fig. 1B).

2.2. Lower Meuse evolution

Due to the good preservation of the Lateglacial river terraces and organic nature of the paleochannel fills, the Meuse valley on the Venlo Block has been extensively investigated. At the start of the Lateglacial, during the Bølling interstadial period (14.7–14.1 ka cal BP), temperature and precipitation increased and the braided river system gradually changed into a low-sinuosity meandering system (Fig. 1B) which coincided with a phase of incision. This transitional system eventually evolved into a high-sinuosity meandering in the following Allerød interstadial period (14.1–12.9 ka cal BP). However, the exact timing of this change is unclear. According to pollen data obtained from the infill of abandoned meander loops, the Meuse started to meander at the start of the Allerød period (Vandenberghe et al., 1994; Kasse et al., 1995; Hoek, 1997). However, bulk ^{14}C data suggest that the meandering system was already active during the Bølling period (Tebbens et al., 1999). During Allerød, the lateral channel migration sediments accreted on the channel point-bar forming up to 7.5-m-thick fining-upward sequences (Van Huissteden and Kasse, 2001). The warm Allerød interstadial is followed by the relatively cold Younger Dryas stadial, during which the Meuse changed to a braided system (Fig. 1B). As a consequence, many of the pre-developed sinuous channels were eroded and only remnant scars are visible at present. Incision of the Lower Meuse during the late Younger Dryas resulted in sediment deflation from terrace remnants and (seasonally) exposed river bars, forming parabolic aeolian dunes on the eastern banks of the river (Fig. 1C) (Bohncke et al., 1993; Kasse et al., 1995). At the transition to the warm Holocene, the braided river system could not continue to exist due to the combined effect of the rapid temperature increase, the decrease in peak discharge and the vegetation recovery. At the start of the Holocene, local permafrost disappeared and the increase of the infiltration capacity of the soil led to lower peak discharges and a higher base flow compared to the Younger Dryas (Van Huissteden and Kasse, 2001). Because of the rapid reforestation during the early Holocene, the sediment supply decreased again and the Meuse river started to incise.

2.3. Allerød-Younger Dryas stratigraphy and core site

In the research area (Fig. 1B), past drilling campaigns revealed that the Allerød-Younger Dryas successions commonly show an abrupt lithological change from Allerød dark-coloured gyttja and organic clay to Younger Dryas grey loam with little organic matter (Fig. 2). In addition, also the established pollen diagrams across the two depositional layers all show the same remarkable change in vegetation composition, i.e., the underlying Allerød *Betula* and *Pinus* phases contrast with the overlying Younger Dryas pollen zone, which is characterized by reduced tree pollen and higher values of non-arboreal pollen taxa (Fig. 2). This indicates that the depositional environments and vegetation types were similar across the study area.

The study site, De Ham, is located in between previously investigated sites (Fig. 1C, Well-Aijen and Ooijen), where we obtained floodplain and levee sediments to reconstruct Holocene flooding stages (Peng et al., 2019; Peng et al., 2020). The De Ham site is located a bit further from the Meuse channel and closer to the Late Pleniglacial terrace (Fig. 1C). The core site is located in an abandoned Lateglacial meander. The complete sinuous shape of the paleochannel is still visible (Fig. 1C). A previous investigation showed that this channel was abandoned in the early Allerød (Van Leeuwen, 2014). After neck cut-off, the paleochannel acted as an isolated fluvial lake. A transect of seven cores with depth of 4–5 m was drilled and six sedimentary units were determined (Van Leeuwen, 2014), mainly based on differences in lithology (Fig. 1D). From the base to the top, the paleochannel infill consists of older sandy terrace deposits (possibly formed in the Bølling period), followed by organic-rich clayey-silty deposits and silty-sandy channel infillings in the upper part (Fig. 1D).

3. Material and methods

3.1. Core description and sampling

The De Ham core was hand-drilled with a gouge in January 2019. The core reached a depth of ~4.2 m. The core was wrapped, and transported to the VU Amsterdam and stored in a cold room at 4 °C. The core contains a 40-cm coarse sequence in the base, followed by a 70-cm, dark coloured, organic-rich interval. Above this is a 190-cm detrital interval with little organic matter, showing a grey and brown colour (among this interval a ~35-cm sand layer was not retrieved in the field). At the top is a ~10-cm peat layer without clastic material (Fig. 3a). In order to obtain a complete sedimentary record, we continuously sampled the core at a 2-cm resolution for grain size and

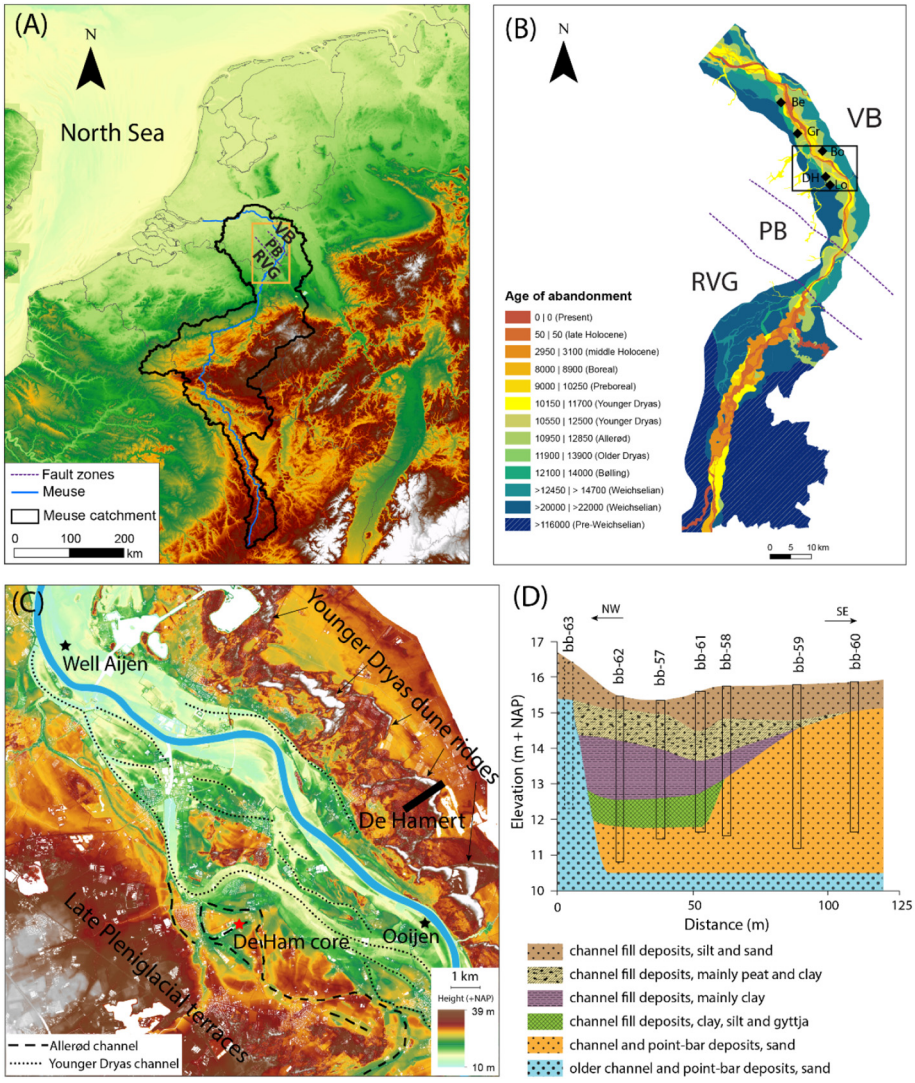

Fig. 1. (A) Digital elevation map showing the Meuse catchment. The square shows the location of panel B. RVG = Roer Valley Graben; PB = Peel Block; VB = Venlo Block. (B) River terraces map of the Lower Meuse catchment (after Woolderink et al., 2018). Black diamonds show the positions of previously investigated cores and also the De Ham core in the Lower Meuse valley. Be = Beugen, Gr = Groeningen, Bo = Bosscherheide, DH = De Ham, Lo = Looiveld. Fig. 2 shows the stratigraphic correlations for these cores. (C) Enlarged digital elevation map of the study area (insert in panel B). The Well-Aijen (floodplain) and Ooijen (levee) sites are investigated in previous studies for Holocene paleoflood reconstructions. De Ham core is located in an Allerød paleochannel which is situated between the present floodplain and the late Pleniglacial terrace. The red star indicates the De Ham core site and the location of the cross section shown in (D). Younger Dryas parabolic dune ridges are located at the east side of the Meuse channel. The black bar shows the sampling transect across the aeolian dunes at De Hamert. (D) Coring transect at the De Ham paleochannel (after Van Leeuwen, 2014). The legend and colours are also used in Figs. 2 and 5 for core lithology. The De Ham core is situated at bb-62.

thermogravimetric analysis, resulting in 148 samples. In addition, we collected 28 samples for pollen analysis and 15 samples for macrofossil analysis throughout the core. We collected another 20 samples from the 380–290 cm depth interval for oxygen ($\delta^{18}O$) and carbon isotope ($\delta^{13}C$) analysis of opercula biogenic carbonate. In order to discriminate fluvial sandy sediments and Younger Dryas aeolian influx in the De Ham core, the De Hamert dune formed in the Younger Dryas (Teunissen, 1983; Bohncke et al., 1993) on the eastern river bank (Fig. 1C) was chosen for sampling. This is because of its proximity to the De Ham core site and its good preservation as evidenced by the parabolic dune morphology (Fig. 1C) and the overlying well-preserved Holocene podzol soil.

3.2. Grain size analysis and end-member modelling

We followed the method described by Konert and Vandenberghe (1997) for sample preparation prior to grain size analysis. For each sample, 10 ml 30% H_2O_2 and 5 ml 10% HCl was used to remove organic matter and calcium carbonates, respectively. After pretreatment, grain-size distributions (GSDs), ranging between 0.1 and 2000 μm were measured with a Sympatec HELOS KR laser-diffraction instrument at the VU Amsterdam.

We used end-member modelling to decompose the GSDs dataset into a certain number of end members (EMs). This approach has been designed to offer the simplest explanation for the observed variations in GSDs in terms of grain-size EM. The obtained EMs can be used to infer provenance and geological processes such as dominant mode of erosion, transport and deposition (Prins et al., 2007; Van Hateren et al., 2018). This is because each EM, derived from a specific setting, corresponding with a certain sedimentological process. For example, Toonen et al. (2015) and Peng et al. (2019) unmixed GSDs from fluvial sediments and assigned the obtained EMs to suspended and bed loads. These components are useful for assessing the water carrying capacity during flooding. Stuut et al. (2002) distinguished the aeolian dust EM from hemipelagic mud EM by unmixing marine sediments

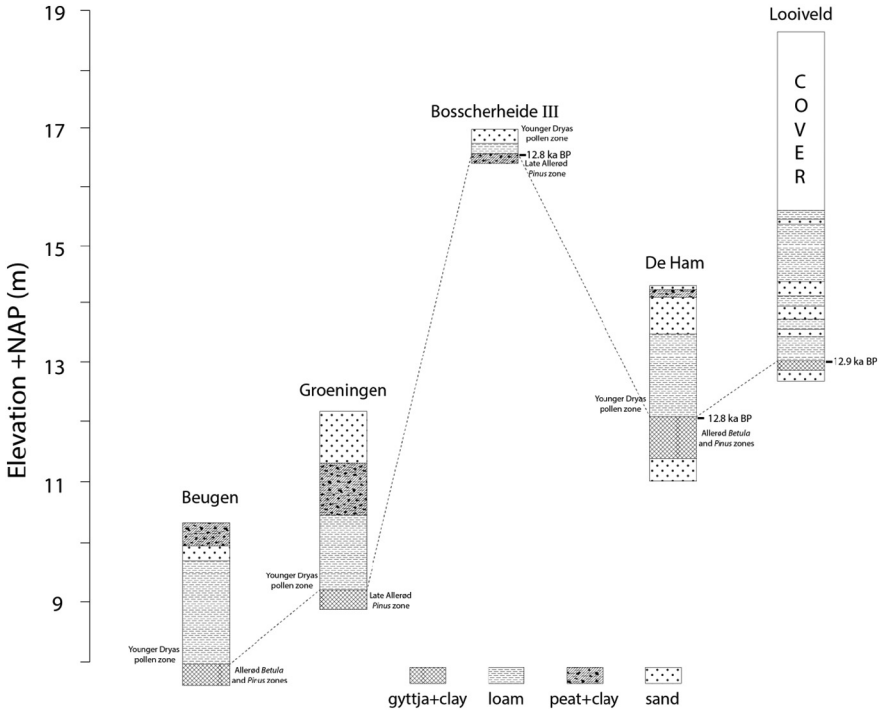

Fig. 2. Lithology and stratigraphic correlations of Late Glacial channel fills in the Lower Meuse valley (see Fig. 1B). The Allerød-Younger Dryas boundary is characterized by abrupt lithological changes from dark-coloured gyttja and organic clay to grey loam with little organic matter. The cores are dated by pollen-based biochronostratigraphical assemblage zones and/or ^{14}C dating. The dashed lines correlate the Allerød-Younger Dryas boundary in each core. The black bars along the cores are ^{14}C dating positions. Beugen (Kasse et al., 1995; Tebbens et al., 1999); Groeningen (Schoffelmeer, 2014; Tebbens et al., 1999); Bosscherheide III (Bohncke et al., 1993; Kasse et al., 1995; Tebbens et al., 1999); Looiveld (Tebbens et al., 1999). Elevation of site Bosscherheide is higher because this site is located on a higher terrace, while other sites are from abandoned Allerød channel fills.

with end member modelling. Prins et al. (2007) concluded two contrasting dust supply patterns over the Chinese Loess Plateau during the last glacial-interglacial cycle. That is, the fine-grained loess EM over the central and southern parts of the Loess Plateau during the interglacial periods and two coarse-grained loess EMs over the northern Loess Plateau mainly during the glacial periods. Therefore, the use of EMs is geo-genetically meaningful and not merely a descriptive methodology. Here, we applied the AnalySize end-member modelling package (Paterson and Heslop, 2015) to the GSDs dataset to obtain the end members. The class-wise r^2 was used to determine the minimum number of end members needed to adequately describe the GSD dataset (Prins and Weltje, 1999; Van Hateren et al., 2018). The end members are used to distinguish bed load versus suspended load subpopulations, which enables the identification of various sub-facies and sedimentary processes.

3.3. Thermogravimetric analysis (TGA)

Thermogravimetric analysis (Heiri et al., 2001) is used to obtain the total organic matter (TOM) content and calcium carbonate content (expressed as loss-on-ignition (LOI)). The mass loss was obtained in a process of stepwise heating from room temperature to 1000 °C. LOI550 (loss-on-ignition at temperature 550 °C) is used to determine the TOM content, and the LOI1000 (loss-on-ignition at temperature 1000 °C) represents the calcium carbonate content.

3.4. Stable isotope analyses

Opercula of the freshwater gastropod *Bithynia tentaculata* were chosen for stable oxygen and carbon isotope analyses in this study. Samples were wet-sieved to remove fine clastic material by using a 63 μm sieve, and the residuals were dried overnight on a 60 °C drying plate. Then the opercula were picked under the stereomicroscope. Since a single operculum represents a time-span of 1–1.5 years, they were homogenized before analysis. The stable $\delta^{13}C$ and $\delta^{18}O$ isotope ratios of the samples were analyzed on a Finnigan MAT 253 Isotope Ratio Mass Spectrometer equipped with Thermo Finnigan Gasbench II at the VU Amsterdam. This apparatus measures the isotopes of CO_2, which is generated by adding few drops of water-free phosphoric acid (100% H_3PO_4) to the samples at a temperature of 45 °C in a clean vial flushed with Helium. The internationally used standard IAEA-603 is measured as a control standard ($n = 10$). The long-term reproducibility for this standard is <0.12‰ and <0.15‰ for $\delta^{13}C$ and $\delta^{18}O$, respectively.

3.5. Pollen and macrofossils analysis

Palynological samples were prepared following the standard methods by Faegri et al. (1989) and Moore et al. (1991). After processing, the residues were mounted on a slide in glycerin for pollen identification and counting at 630× magnification. The pollen taxa include trees, shrubs, upland and wetland herbs and aquatics. The percentage pollen diagram was made using the Tilia software package (Grimm, 1992; Grimm, 2004).

Prior to macrofossil analysis, fifteen samples were heated in a 5% KOH solution near boiling point for 10–15 min and subsequently washed through a 150 μm mesh sieve. The sample material was systematically examined at 15-40× magnification under a stereomicroscope. Seeds, fruits, leaves and other remains of interest were picked and determined. Macrofossil finds are presented as presence/absence data. The diagram was constructed using the Tilia software package (Grimm, 1992; Grimm, 2004).

3.6. AMS ^{14}C dating and age model

AMS ^{14}C dating was performed at Beta Analytic testing laboratory, Miami (USA). Seeds from different terrestrial species and wood pieces

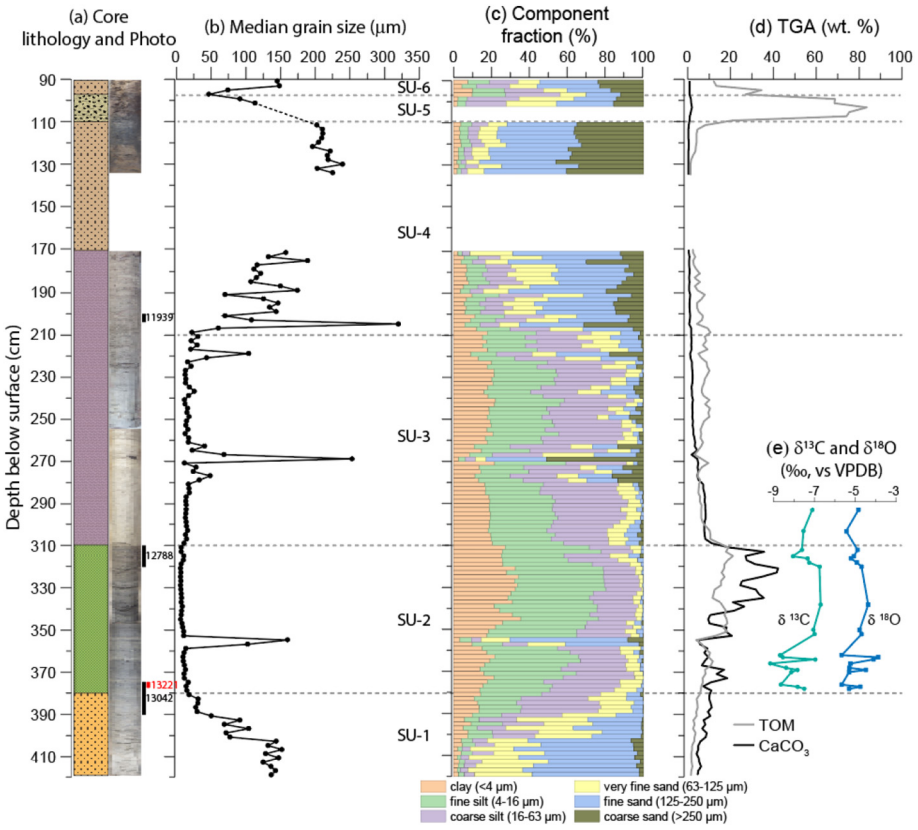

Fig. 3. Sedimentary results of De Ham core. Dashed lines separate sedimentary units (SU). (a) core lithology and photo; vertical bars along the core photo represent the dated interval and calibrated ^{14}C dating results (see Table 1); (b) median grain size; (c) grain size distribution, with size fraction classification cf. Wentworth (1922); (d) total organic matter (TOM) and calcium carbonate ($CaCO_3$) content; (e) oxygen and carbon isotope variations of the opercula biogenic carbonate.

were selected for ^{14}C dating (Table 1). Because the amount of datable material in the 2-cm interval samples was limited, seeds from several adjoining samples were combined to meet the (least required mass) requirements for AMS dating (Table 1). In addition to AMS dating, additional age-control points were derived from the pollen data through correlation with the regional pollen biochronostratigraphy. In the Netherlands, the vegetation history since the Lateglacial has been well studied (Bohncke et al., 1987; Van Geel et al., 1989; Hoek, 1997; Hoek and Bohncke, 2002; Hoek et al., 2017). These results provide a solid reference for biostratigraphic correlation. The pollen assemblage zones in this study were correlated with the established regional pollen zones (see Table 2 in Hoek, 1997), which were compiled on the basis of over 250 palynologically investigated sites relating to the Lateglacial period. In the end, all chronological information was integrated to construct the age-depth model of the De Ham core (see Section 4.3.2).

4. Results

4.1. Sedimentary characteristics, grain size, TGA and isotope results

Based on the integrated sedimentary results, including core lithology (which is related to sedimentary facies), median grain size, grain-size distribution, organic matter and carbonate content, we divided the De Ham core into six sedimentary units (SU hereafter).

SU-1 (420–380 cm) - This unit represents the lower part of channel infill, consisting of grey silts and sands with a fining-upward trend. The colour of this interval gradually changes upwards from medium grey to dark grey (Fig. 3a). There is no clear lamination in this interval. The median grain size decreases from ~140 μm at the lower part to 17 μm at 380 cm (Fig. 3b). Sand is the dominant component near the base of the core, with a clear transition to silt-dominated sediments in the upper half of SU-1 (Fig. 3c). The total organic matter (TOM) and calcium carbonate content increase gradually to 5% and 10%, respectively (Fig. 3d). The fining-upward trend is reflected in the GSDs, the major mode of which shifted from 100-180 μm to ~50 μm (Fig. 4a).

SU-2 (380–310 cm) - This unit is distinguished from SU-1 by its fine-grained grain-size characteristics. The unit consists of laminated silty and clayey sediments, exhibiting a dark colour with embedded organic laminae (Fig. 3a). The median grain size has a consistently low value (<10 μm), except at 355 cm where a ~4-cm thick sandy layer is present with median grain size of 160 μm (Fig. 3b). The clay and fine silt proportions increase to the maximum level of 30% and 50% in this unit, respectively (Fig. 3c). The TOM and calcium carbonate content increase respectively to 20% and 42% at the dark organic-rich gyttja interval (350–310 cm) (Fig. 3d). Through the De Ham core, opercula were only present in the interval between 378 and 293 cm. $\delta^{18}O$ values of the opercula range from −5.66 to −3.87‰ and $\delta^{13}C$ values range from −9.2 to −6.7‰ (Fig. 3e). The most negative excursion of $\delta^{18}O$ (between −5.6‰ and −4.8‰) and $\delta^{13}C$ (between −9.2‰ and −7.5‰) occurs at 380–360 cm. The GSDs have unimodal ranging between 7 and 12 μm except at 355 cm and 357 cm where the modes shifted to 180 μm (Fig. 4b).

SU-3 (310–210 cm) – The boundary between SU-2 and SU-3 is characterized by a sharp lithological change. The homogeneous sediments show a grey colour and organic fragments are observed occasionally. The median grain size shows only a slight increase at 310 cm. In the coarser intervals, between 281- 261 cm and at 220

Table 1
AMS ^{14}C dating results and calibrated ages with 2σ standard deviation.

Lab code	Depth (cm)	^{14}C ages (year BP)	Cal. range (year BP)	Cal. median (year BP)	Dated materials
Beta-535687	204–200	10,220 ± 30	12,095–11,775	11,939	*Betula* seeds
Beta-535686	320–310	10,950 ± 40	12,929–12,710	12,788	Seeds of *Betula*, *Filipendula*, *Carex*, *Apiaceae*, *Heracleum*
Beta-535685	376–374	11,380 ± 40	13,306–13,124	13,221	Wood fragment
Beta-535684	390–374	11,160 ± 40	13,112–12,922	13,042	Leaf fragments and seeds of *Betula*, *Filipendula* and *Carex*

cm, the median grain size reaches values of up to 250 μm and 123 μm, respectively (Fig. 3b). Clay and silt are the dominant fractions, accounting for ~20% and ~65%, respectively, with the total sand fraction showing considerable variations (Fig. 3c). At the transition of SU-2 and SU-3, both the TOM and calcium carbonate content decline abruptly (Fig. 3d). The modes of the GSDs vary between 10 and 30 μm, except in the interval of 281–261 cm and at 220 cm, in which the modal size ranges between 200-300 μm and 250 μm, respectively (Fig. 4c). The colour change (from light brown to grey) at 255 cm (Fig. 3a) is related to the variable light conditions in the field, and does not reflect a real lithological change.

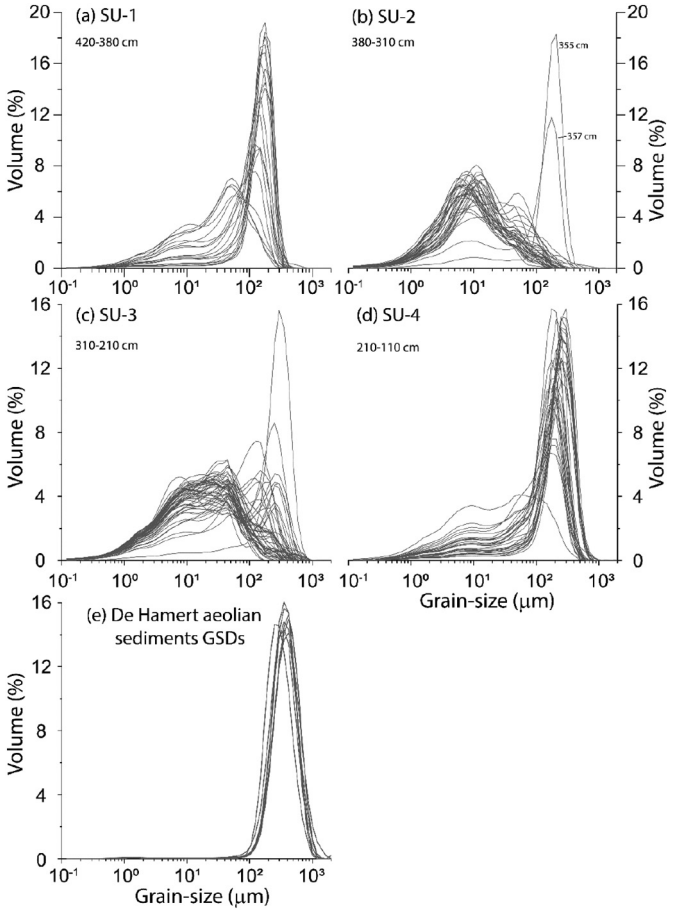

Fig. 4. Grain size distributions (GSDs) of the sediments in SU 1–4 in De Ham core and De Hamert aeolian sediments. The major mode in SU-1 shifted from 100-180 μm to ~50 μm, representing a fining-upward trend. In SU-2, the mode range changes to 7–12 μm except at 355–357 cm. In SU-3, the modes of sediments range at 10–30 μm, except in the 281–261 cm and ~220 cm intervals in which the modes range at 200–300 μm and 250 μm, respectively. In SU-4, the GSDs have a bimodal pattern, with a variable coarse mode at 180–300 μm and a minor one at ~10 μm. The aeolian sediments show a unimodal pattern with the mode at 250–420 μm.

SU-4 (210–110 cm) - This unit is characterized by its brown coarse-grained, sand-dominated sediments (Fig. 3a). The sediments mainly consist of silts and sands, and millimetre-sized coarse sand grains are observed. The grain size of the missing sandy interval is unknown, but it is comparable with its adjacent layer, according to the field notes. The median grain size increases from 26 μm at 210 cm to 250 μm at 130 cm (Fig. 3b). The silt fraction gradually reduces upwards to 10%, and the sand component rises to about 80% (Fig. 3c). The TOM (<10%) and calcium carbonate content (<5%) reach their lowest values in this unit (Fig. 3d). The GSDs show a bimodal pattern in this interval, with a finer mode at ~10 μm and a variable coarse mode at 180–300 μm (Fig. 4d).

SU-5 (110–97 cm) - This unit is a peat layer (Fig. 3a) and has nearly no clastic grains. The TOM reaches to a maximum of 84% in this interval while the calcium carbonate is low (Fig. 3d).

SU-6 (97–90 cm) - This unit consists of silty sands with organic matter content of 10–30% (Fig. 3c, d).

The GSDs of De Hamert aeolian sediments exhibit unimodal pattern and have well-defined modes in the range 250–420 μm (Fig. 4e). This information will be used as a fingerprint of aeolian sediments (see Section 5.2.1).

4.2. End-member modelling results

The end-member modelling results show that a four-end-member model is capable of reproducing ~90% of the total variance in the GSD dataset (Fig. 5a). A three-end-member model performs poorly in the range of 30–80 μm, while a five-end-member model is unable to significantly improve the modelling performance (Fig. 5b). To comply with the principle of parsimony (Weltje, 1997; Prins, 1999), the four-end-member model is adopted in this study. The four end members have a unimodal GSD with different modal sizes. EM1 and EM2 have modes at 9 and 53 μm, respectively (Fig. 5c). EM3 and EM4 are coarser than EM1 and EM2, and have modes at 170 and 300 μm, respectively (Fig. 5c).

The cumulative percentages of the four end members are plotted against core depth in Fig. 5d. In SU-1, the EM3 is dominant but it reduces from ~90% at the base to less than 10% at the top (Fig. 5d). In the upper organic-rich part of SU-2, the EM1 proportion increases to 95% at the expense of EM2 (Fig. 5d). In SU-3, EM1 (~50%) and EM2 (~30%) both show a relatively constant proportion while the proportion of EM3 and EM4 fluctuates (Fig. 5d). In SU-4, the abrupt coarsening at ~210 cm is reflected by the sharp increase in EM4 and EM3 (Fig. 5d).

4.3. Vegetation development and biochronostratigraphy

4.3.1. Pollen and macrofossil analysis

The pollen diagram is given in Fig. 6. Arboreal pollen (AP) taxa include all trees and *Humulus*, *Hedera* and *Juniperus* shrub taxa. Of the non-arboreal pollen taxa (NAP) only the upland herb taxa are used, in order to avoid overrepresentation of local wetland (i.e., marsh and aquatic) NAP-taxa. The AP/NAP-ratio reflects the varying degree of openness of the upland paleo-vegetation. Ericales (*Empetrum* and Ericaceae) have been placed separately in the AP/NAP-ratio diagram.

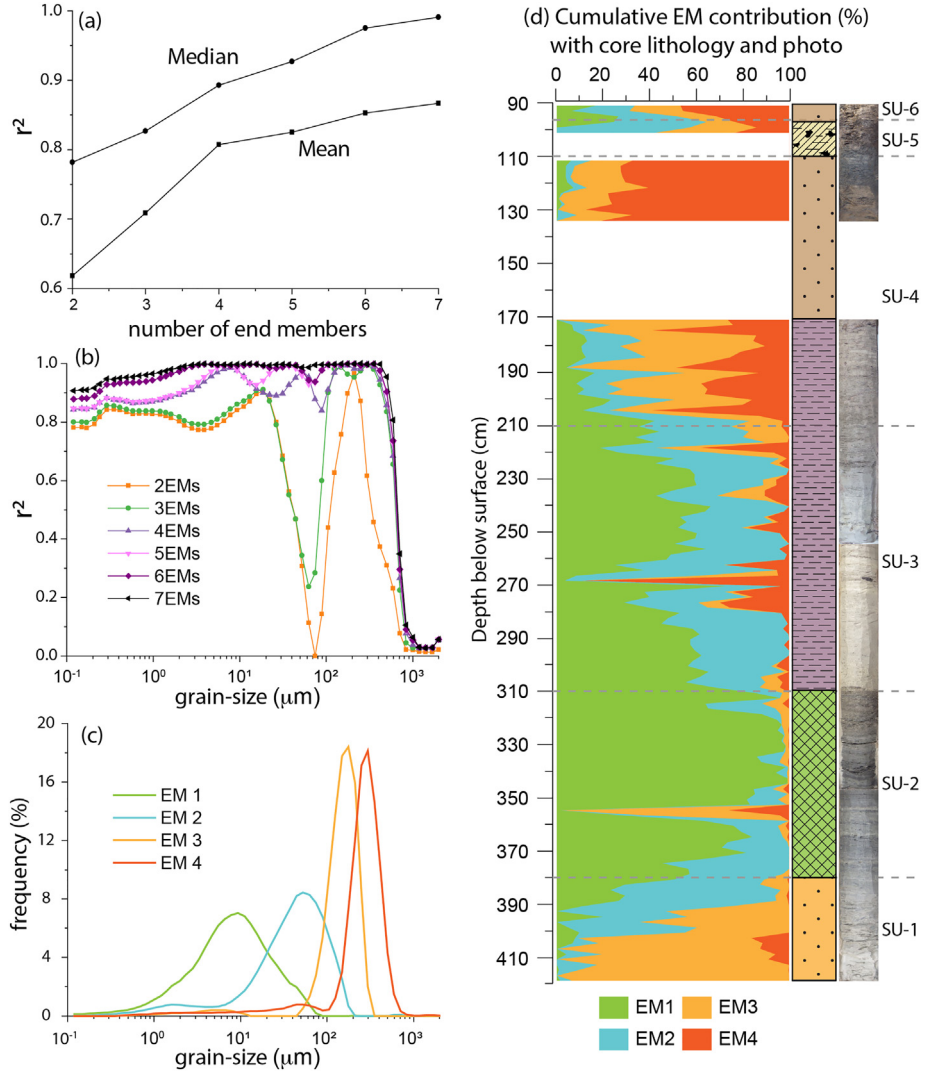

Fig. 5. End member modelling results. (a) Median and mean r^2 on all grain size classes as a function of the number of end members. A four-end-member model is capable of explaining >90% of the total variance; (b) r^2 for each size class for end-member models with two to seven end members; (c) the modelled end members according to the four-end-member model; (d) proportional contribution of the EMs of the 4EMM with core lithology and photo.

The pollen sum was defined as the sum of all trees, shrubs and the upland herbs. Wetland plants, aquatic plants and algae were excluded as these taxa are of local origin. Based on changes in the pollen assemblages, we divided the diagram into seven local pollen assemblage zones (LPAZ).

LPAZ-1 (400–365 cm) features high *Betula* and low *Pinus* percentages. The NAP taxa have high percentages at the base of LPAZ-1 and decline rapidly upwards (Fig. 6).

LPAZ-2 (365–310 cm) shows high *Pinus* and *Betula* percentages while *Salix* declines. The wetland herbs increase and the NAP percentages are low (Fig. 6).

In LPAZ-3 (310–230 cm), percentages of AP decrease while those of NAP increase steadily, including taxa such as Poaceae, *Artemisia*, Asteraceae tub. and Asteraceae lig. Most wetland herbs gradually reduce except Cyperaceae (Fig. 6).

In LPAZ-4 (230–180 cm), the percentage of *Pinus* slightly declines while *Betula* increases. Open land species like *Empetrum* and Ericaceae appear in this zone, together with upland herbs like Asteraceae, *Helianthemum*, Brassicaceae and *Rumex* (Fig. 6). *Polemonium*, a subarctic species that indicates an open landscape, occurs for the first time in this zone.

In LPAZ-5 (180–120 cm), the pollen record shows continuity in the species composition, despite the missing sandy interval (170–135 cm). The pollen diagram shows a decline of *Betula* and a strong increase of *Pinus*. Low percentages of *Corylus*, *Alnus*, *Tilia* are related to soil formation and bioturbation in the top of the sand layer. The amount of Poaceae declines, and a small *Juniperus* peak is observed at the start of LPAZ-5, marking the start of stabilization of the landscape. *Empetrum* and Ericaceae have disappeared.

LPAZ-6 (120–105 cm) has high AP values. The amount of *Pinus*, shrubs and upland herbs declines, and the amounts of *Betula*, *Corylus* and *Quercus* show an increase.

In LPAZ-7 (above 105 cm), the percentages of *Alnus*, *Quercus*, *Ulmus* and *Tilia* have their highest values. The NAP taxa (shrubs and upland herbs) reach their lowest percentages (Fig. 6).

Based on a selection of in-lake taxa present in the De Ham core, three macrofossil assemblage zones (MAZ) were distinguished (Fig. 7). MAZ-1 (390–310 cm) is characterized by the presence of *Bithynia tentaculata*

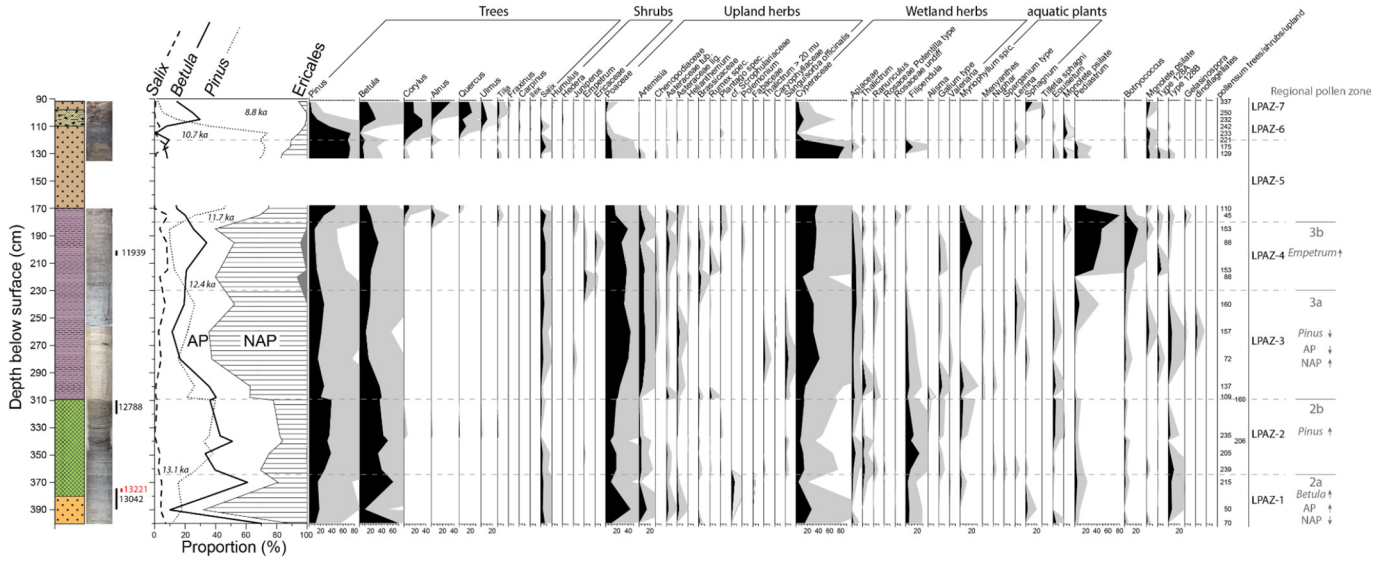

Fig. 6. Pollen diagram of the De Ham core. From left to right are core lithology and photo, arboreal pollen (AP including all trees and *Humulus*, *Hedera* and *Juniperus* shrub taxa) and non-arboreal pollen (NAP including the upland herb taxa). The *Ericales* curve represents *Empetrum* plus *Ericaceae*. The diagram is divided into seven pollen zones; numbers in the main AP/NAP diagram above the dashed lines are additional age points derived from Hoek (1997) (see Section 4.3.2 and regional pollen zones at right side).

opercula, *ostracods* and carbonate precipitation (Fig. 7). Aquatic plants (macrophytes) such as Nymphaeaceae and *Potamogeton* spp. together with *Cristatella mucedo* (Bryozoa statoblast) are present over the complete MAZ-1. MAZ-1 can be subdivided into two subzones: 1a and 1b, based on the first occurrence of *Gloeotrichia* type and Characeae at 350 cm depth. In the top part of subzone 1b, *Myriophyllum spicatum* and *Hottonia palustris* appear (Fig. 7). At the transition to MAZ-2 (310–230 cm), *Gloeotrichia* type, *Myriophyllum spicatum* and *Hottonia palustris*

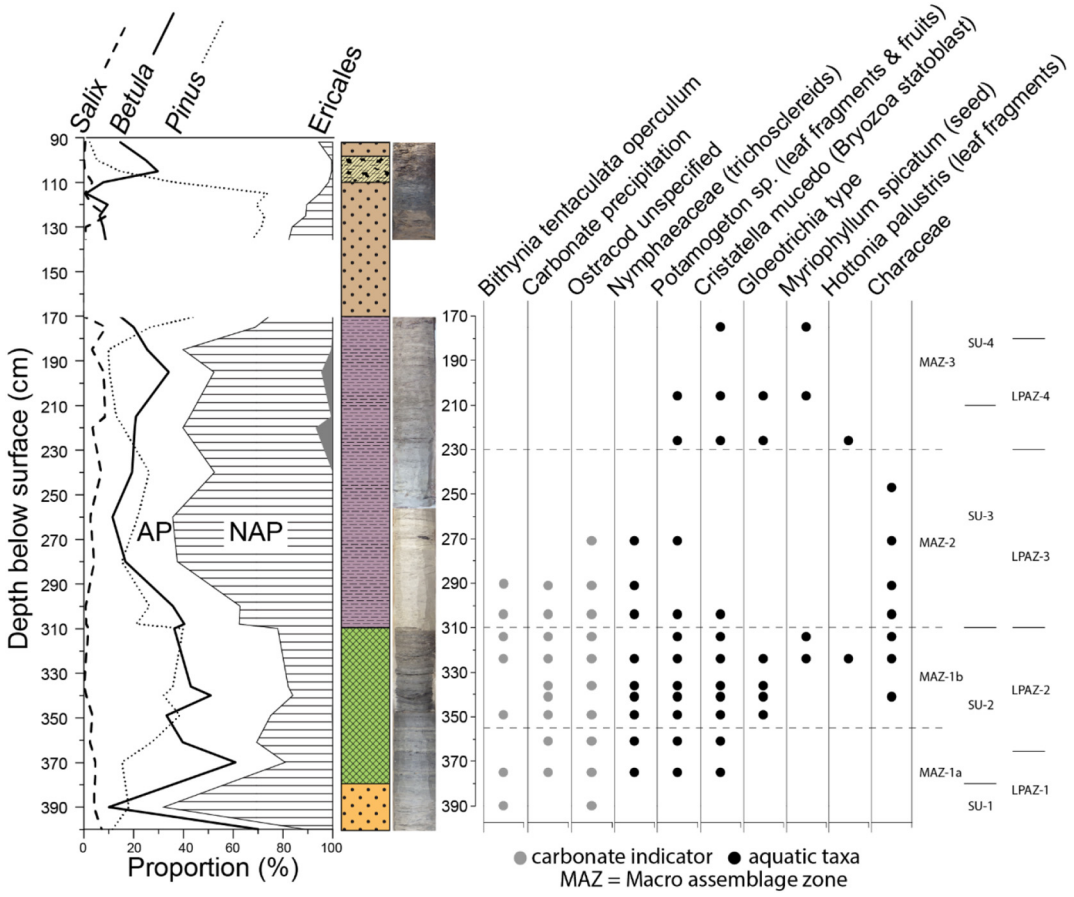

Fig. 7. Macro fossil diagram of the in-lake taxa (in black) of the De Ham core, expressed as presence/absence. In grey we show the carbonate indicators. Sedimentary units (SU) and local pollen assemblage zones (LPAZ) are shown at right side for comparison.

disappear. *Bithynia tentaculata*, *ostracods* and carbonate precipitation, as well as Nymphaeaceae and *Potamogeton* are present until 290 cm and 270 cm depth, respectively. Characeae are present throughout this zone (Fig. 7). In MAZ-3 (230–170 cm), *Potamogeton*, *Cristatella mucedo* (Bryozoa statoblast), *Gloeotrichia* type, *Myriophyllum spicatum* and *Hottonia palustris* reappear while Characeae disappear (Fig. 7).

4.3.2. Chronological model-results from biostratigraphic interpretation

The AMS ^{14}C dates were calibrated using the IntCal13 curve (Reimer et al., 2013). The dating results are listed in Table 1. AMS ^{14}C dates from 390–374 cm, 376–374 cm, 320–310 cm and 204–200 cm provide ages of *c.* 13.0 ka cal BP and 13.2 ka cal BP, 12.8 ka cal BP and 11.9 ka cal BP, respectively (Table 1, Fig. 3a). These dates indicate that most of the De Ham core sediments were deposited during the Allerød and Younger Dryas. The aquatic plant and fauna taxa (Figs. 6, 7), together with the presence of clayey sediments (Fig. 3a) show that the core site was a lake environment in the interval 390–170 cm. LPAZ-1 and LPAZ-2 represent regional vegetation conditions during the Allerød, as confirmed by the AMS dating (Fig. 6). These pollen zones roughly correspond with MAZ-1a and 1b, respectively (Figs. 6, 7). The low pollen sum in LPAZ-1 is associated with the nature of the sandy deposits (Fig. 3a, c). The increased pollen sum in LPAZ-2 reflects a high preservation capacity and lake level during the late Allerød. MAZ-1a is indicative of shallow fresh-water lakes/ponds. *Myriophyllum spicatum*, *Hottonia palustris*, Characeae and carbonate precipitation are indicators of calcareous water conditions (Streeter et al., 2016).

According to the variation and relative abundance of pollen taxa, LPAZ-1 and LPAZ-2 correspond with zone 2a (Allerød *Betula* phase) and 2b (Allerød *Pinus* phase) of Hoek (1997) (Fig. 6). The correlation of the regional pollen diagram with the Greenland GISP2 ice core shows that the transition from zone 2a to 2b occurred at ~13.1 ka cal BP (Hoek, 1997). Considering the AMS ^{14}C dates above (12.8 ka cal BP) and below (13.2 ka cal BP) the boundary of LPAZ-1 and LPAZ-2, it is reasonable to assume an age of 13.1 ka cal BP for this boundary (Fig. 6), and this also indicates that the ^{14}C date from interval 390–374 cm is slightly too young.

Both LPAZ-3 and LPAZ-4 feature reduced AP (*Betula* and *Pinus*) and high NAP (i.e., appearance of *Artemisia* and Asteraceae) while *Empetrum* and Ericaceae only appear in LPAZ-4 (Fig. 6). The characteristics of the two zones correspond well with the regional zones 3a and 3b of the Younger Dryas (Hoek, 1997) (Fig. 6). The disappearance of *Myriophyllum spicatum* seeds and *Bithynia tentaculata* opercula in MAZ-2 might suggest a temperature decrease, as *Myriophyllum* needs an optimum July temperature of >10 °C, and *Bithynia tentaculata* is frost sensitive (Gittenberger et al., 2004; Gaillard and Birks, 2007). The increased percentages of upland herbs in LPAZ-4 (Fig. 6) indicates a more open landscape, i.e., the appearance of *Polemonium* reflects a subarctic environment. In LPAZ-4, the high percentages of wetland herbs and consistent presence of *Myriophyllum* in both the pollen and macrofossil data (Figs. 6, 7) indicate that the core site was still a lake during the late part of the Younger Dryas. Based on these observations, we argue for a two-phase Younger Dryas climate pattern in the Lower Meuse catchment which is reflected by LPAZ-3 and LPAZ-4. The proposition of a two-phase Younger Dryas has been suggested previously from multiproxy climate data for Western Europe (Isarin et al., 1998; Isarin and Bohncke, 1999; Schenk et al., 2018). In more detail, it is suggested that a relatively cold and humid phase was followed by a dry phase (i.e., Isarin et al., 1998; Muschitiello et al., 2015; Hepp et al., 2019), although an opposite pattern (a drier early Younger Dryas) has also been proposed (i.e., Brauer et al., 1999; Brauer et al., 2008). We adopted an age of 12.4 ka cal BP based on the transition between zones 3a and 3b from Hoek (1997) for the boundary of LPAZ-3 and LPAZ-4 here (Fig. 6), and this seemingly agrees well with the AMS ^{14}C dating results of 12.8 ka cal BP at 320–310 cm and 11.9 ka cal BP at 204–200 cm in the De Ham sequence.

The decline of NAP and Ericales and increasing *Pinus* values at the base of LPAZ-5 (Fig. 6) mark the onset of the Holocene (Preboreal, 11.7–10.7 ka cal BP). The AP taxa increase at the expense of shrubs and upland herbs (Fig. 6), indicating a restoration of the forest. The low values of *Corylus*, *Alnus*, *Querus* and *Tilia* (Fig. 6) seem to imply that the lower part of LPAZ-5 corresponds to the Atlantic period, as these taxa are common since the middle Holocene and they are absent in regional pollen diagrams of the early Holocene (cf. Iversen, 1973; Hoek, 1997; Bos et al., 2007; Hoek et al., 2017). However, we interpret these low percentages as the result of soil formation and/or bioturbation (i.e., plant root penetration and burrowing), as was observed during sampling of the sandy interval. Based on these observations, we suggest that the boundary of LPAZ-4 and LPAZ-5 is the transition of the Lateglacial to the Holocene period at *c.* 11.7 ka cal BP (Fig. 6), in accordance with Hoek (1997). In LPAZ-6, *Corylus*, *Quercus* and *Ulmus* start to increase, and *Pinus* is decreasing. Shrubs and upland herbs are nearly absent, resulting in high percentages of AP taxa. In addition, the increased pollen sum (Fig. 6) implies a dense vegetation cover. This zone corresponds to the Boreal period (10.7–8.8 ka cal BP) in the regional vegetation development (Iversen, 1973). The high values of *Quercus*, *Alnus*, *Tilia* and *Ulmus*, and low values of *Pinus* and *Betula*, together with the shrubs and herbs observed in LPAZ-7, correspond with Holocene vegetation reconstructions in the Lower Meuse (Kasse et al., 1995; Bos and Zuidhoff, 2015) and also with the NW European pollen zones. Based on this, we interpret the base of LPAZ-7 as the start of the Atlantic period (8.8–5.6 ka cal BP). The obtained time boundaries based on the regional biostratigraphy, together with the AMS ^{14}C dating were used to establish a chronological model (Fig. 8a). Accordingly, the sedimentation rate is calculated based on the age model (Fig. 8b).

5. Discussion

5.1. Paleoclimate in the Lower Meuse catchment during the Allerød and Younger Dryas

The core site is situated in an oxbow lake which is close to the active channel (Fig. 1C). During the Allerød period, the meandering river more or less flowed at the same height level (no incision) because of a regular discharge (Kasse et al., 1995; Woolderink et al., 2018). These two factors resulted in a high groundwater table and therefore, both flooding water and groundwater were important sources to the shallow lake. In this shallow lake setting, the preserved calcium carbonate content in sediments relies on its precipitation and dissolution rate:

$$Ca^{2+} + 2HCO_3^- \leftrightarrow CaCO_3 + CO_2 + H_2O \quad (1)$$

The calcium carbonate precipitation is primarily dependent on the bicarbonate content of the groundwater feeding the lake. Assuming a relatively constant bicarbonate content of the ground water, the authigenic carbonates are commonly precipitated by warming and/or photosynthetic utilization of CO_2 resulting in calcium carbonate supersaturation in the water column. In most temperate high-latitude regions authigenic carbonates are precipitated mainly in summer during periods of maximum warming and phytoplankton productivity. Furthermore, the amount of evaporation has a major influence on the isotope composition of standing water bodies, especially in small-scale lakes (Leng et al., 1999; Teranes and McKenzie, 2001; Leng and Marshall, 2004). In this case, the temporal variation of calcium carbonate content can serve as a proxy of paleo-temperature and lake productivity (Stuiver, 1970; Roberts et al., 2008). *Bithynia tentaculata* is a common freshwater prosobranch gastropod with a life span of one to three years, although growth may stop after the first year (Fretter and Graham, 1976; Graham, 1988). Therefore, analyzing the biogenic carbonates from opercula of *Bithynia tentaculata* can provide years-average $\delta^{18}O$ and $\delta^{13}C$ values that are generally ascribed to variations

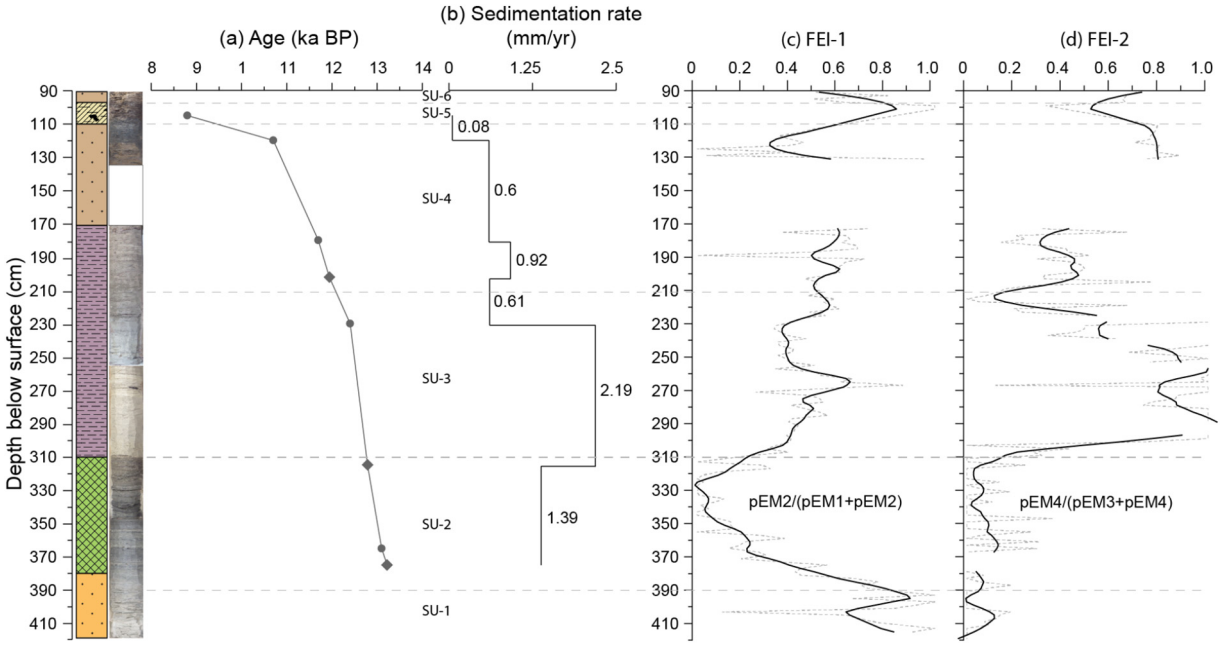

Fig. 8. (a) Linear age model based on the AMS ^{14}C dating (diamonds) and pollen-based biostratigraphical correlation (dots); (b) sedimentation rate; (c–d) flood energy indexes calculated after the end member modelling analyses on the grain size dataset. The dotted grey lines are raw data, and solid black lines are processed curves by using a locally estimated scatterplot smoothing method to prevent undue emphasis being placed on single data. The interruptions in (d) indicate intervals where no valid data points are present.

in temperature and precipitation isotope composition (Leng and Marshall, 2004).

In the Allerød 13.2–12.7 ka cal BP interval, a covariation of calcium carbonate with $\delta^{18}O$ and $\delta^{13}C$ is observed (Fig. 9a). The high (low) calcium carbonate content values correspond with heavier (lighter) $\delta^{18}O$ and $\delta^{13}C$. During the Allerød, both photosynthesis and evaporation were higher during the summer than in winter time in this small-scale lake. Stronger photosynthesis promoted the uptake of CO_2 by vegetation that led to carbonate super-saturation in the water column (see Eq. (1)), and depletion of ^{12}C and enrichment of ^{13}C in the lake because the photosynthetic organisms prefer using ^{12}C in lake water (Meyers and Teranes, 2002). The former resulted in higher calcium carbonate precipitation and the latter explains enrichment of ^{13}C in biogenic carbonate (Fig. 9a). Meanwhile, high evaporation in summer caused heavier oxygen isotope left in the lake (Fig. 9a). This explanation indicates a dominant evaporation effect in the lake during the Allerød. The observations imply a dynamic response of the sedimentary environment to the local climate.

The more negative excursion in the $\delta^{18}O$ record and lower TOM and calcium carbonate content in the De Ham core at around 13.1 ka BP correspond with the intra- Allerød Cold Period, a cold climatic reversal observed in GISP2 ice-cores (Stuiver and Grootes, 2000) (Fig. 9b). Warmer climate conditions during the Late Allerød are reflected both in the ice-core oxygen isotope records and by generally high $\delta^{18}O$ and $\delta^{13}C$ values in the De Ham core (Fig. 9a, b). The decreased AP/NAP values (indicating a degraded tree cover), TOM and calcium carbonate content (Fig. 9a) indicate a fast response of the environment to the climate change at the Allerød-Younger Dryas transition. Overall, the positive correlations between the De Ham core sedimentary proxies and Greenland ice core oxygen isotope records imply a direct link between the Lower Meuse paleoenvironment and North Atlantic climatic oscillations during the Lateglacial.

5.2. Floods in the Lower Meuse catchment during the Allerød-Younger Dryas

5.2.1. Interpretation of the end-member mixing model

The De Ham core contains sediments that were deposited during the Allerød, Younger Dryas and early to middle Holocene. Previous studies have pointed out important aeolian activity in this area during the Younger Dryas, as a result of a degraded vegetation cover (Kasse et al., 1995; Huisink, 1997; Kasse, 2002; Kolstrup, 2007) and strong and stable westerlies (Renssen et al., 1996; Brauer et al., 2008). Therefore, in addition to flood sediments, aeolian sediments could also have been deposited at the core site. Hence, a reliable interpretation of the sediment source is vital to reconstruct the Lateglacial flood record of the Lower Meuse.

The grain size information of the De Ham core sediments and the unimodal-pattern of the GSDs of the De Hamert aeolian sediments (Fig. 10b) can be used to differentiate aeolian from fluvial sedimentary components in the De Ham core. The distinct grain size distributions of the two fine end members (EM1 and EM2) from the two coarse end members (EM3 and EM4) indicate different deposition processes represented by the two groups. EM1 and EM2 mainly occur in SU2–3, in which the sediment components are dominated by clay and coarse silt (Fig. 3c). The total sum of EM1 and EM2 in these two units adds up to more than 85% (Fig. 5d). Therefore, we interpret both EM1 and EM2 as suspended load sub-populations. The grain size range of these two end members fall in the range of the suspended load components found at the Well-Aijen and Ooijen sites (Fig. 10c, d). Although units SU-2 and SU-3 contain Lateglacial sediments while the Well-Aijen and Ooijen sites contain Holocene sediments, the resembling GSDs of the suspended load in the De Ham core and the Well-Aijen floodplain core (Fig. 9a, c) imply that the sedimentary processes (sediment source, transport and deposition) have resulted in very similar suspended load components. However, the different shapes of the GSDs of the fine EMs (suspended load) between Well-Aijen and Ooijen (Fig. 10c, d) indicate the sedimentary setting (floodplain versus levee) determines suspended load sorting, despite the proximity of the two sites and concurrent sedimentation therein. Similarly, the coarse-grained EM3 and EM4 resemble the coarser EMs from the Well-Aijen and Ooijen sites and also the De Hamert dune sands (Fig. 10b–d) and thus can be associated with fluvial bed load deposits or aeolian influx.

The sediments in SU-1 were deposited shortly after channel abandonment, and the dominant EM3 in this unit represents the fluvial bed load component (Fig. 5d). Aeolian activity in the Allerød was

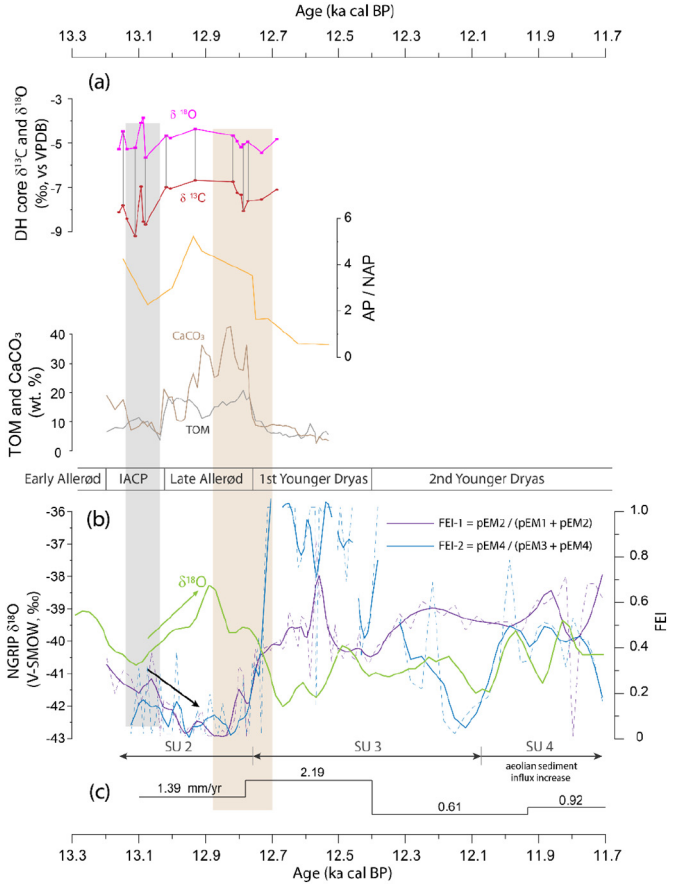

Fig. 9. De Ham sedimentary record and reconstructed Lateglacial floods at the Allerød and Younger Dryas periods. (a) $\delta^{18}O$ and $\delta^{13}C$ of the opercula biogenic carbonate, AP/NAP, TOM and calcium carbonate content records show apparent variations during the Allerød and the transition to the Younger Dryas; (b) comparison of the two flooding energy indexes and NGRIP ice core ^{18}O records; solid lines = smoothened FEI results, dashed = raw results. (c) Sedimentation rate. Grey and brown shaded areas show the intra-Allerød Cold Period and Allerød-Younger Dryas transition period, respectively.

probably limited because the land surface was largely covered by pine-birch forest and shrubs (Fig. 6). The high soil stability reduced aeolian sediment availability. Therefore, the relatively high sedimentation rate of 1.39 mm/yr (Fig. 8b) in SU-2 should be the result of flooding. In SU-3, EM1 and EM2 are the major grain size subpopulations, and only spikes of EM3 and EM4 occur (Fig. 5d). The fine-grained sediments in this unit cannot be related to aeolian-dominated sedimentation. The disappearance of *Cristatella mucedo* (Bryozoa statoblast), *Myriophyllum spicatum*, *Hottonia palustris* in MAZ-2 of SU-3 might be due to an increased turbidity of the lake water, e.g. a higher suspended sediment load, related to higher peak discharges and increased flooding. Reduced soil water storage capacity, development of permafrost and more snow accumulation in the colder winters during the Younger Dryas favoured a higher peak discharge and severe flooding during spring (Kasse et al., 1995), and this could explain the spikes in the EM4 record in SU-3 (with mode at 300 μm) (Fig. 5d). We conclude that the sediments in SU-3 were derived mainly from floods. In SU-4, the sediments are much coarser, with high proportions of EM3 and EM4 (Fig. 5d). At 210–170 cm, EM4 shows a background value (the minimum level) of 15% and the EM3 proportion is ~40% (Fig. 5d). In the context of a gradually infilled abandoned channel, more open vegetation conditions (Fig. 6), reduced soil water capacity and enhanced westerlies and higher peak discharge (Kasse et al., 1995; Renssen et al., 1996; Brauer et al., 2008), we suggest that the coarse sediment at 210–170 cm includes both flood and aeolian sandy sediments. In addition, the contribution from aeolian activity probably became dominant starting from the base of SU-4 (at ~207 cm). The dominance of EM4 above 134 cm cannot be related to aeolian input, because during the Holocene vegetation recovered and aeolian activity was largely reduced in the Lower Meuse. Sediment reworking or a more local fluvial process should be responsible for deposition of these sandy sediments.

5.2.2. Lateglacial flood reconstruction for the Lower Meuse

Previous Holocene paleoflooding reconstructions for the Lower Meuse based on Well-Aijen floodplain and Ooijen levee sediments (Fig. 1C) relied on highlighting the coarse components among fine and coarse end members (Peng et al., 2019; Peng et al., 2020). Sediments from the De Ham core are composed of very similar fine and coarse components (Fig. 3b, c). In the fluvial sediment-dominated interval (420–207 cm), EM1 and EM2 can be interpreted as suspended load components and EM3 and EM4 as bed load components. This interpretation conforms to the mixing model proposed by Erkens et al. (2013) for the lower Rhine catchment, and to Peng et al. (2019) and Peng et al. (2020) for the Meuse catchment. Based on the principles of the latter two studies, we construct two flood energy indexes (FEI) that independently highlight the coarse components within the suspended load fraction (EM1 and EM2) and the bed load fraction (EM3 and EM4). Because the depth and velocity of the past flood water are unknown, a precise calculation of the kinetic energy of the paleoflood is not possible. Here, the flood energy does not mean the kinetic energy of the water. Instead, we use this index to reflect the capacity of floods to transport sediment. The key function of defining these two indexes is that they, independently from each other, amplify the flooding signal contained within the suspended load and bed load sediment fractions. The two indexes are expressed as:

$$\mathrm{FEI}-1 = \frac{pEM2}{(pEM1 + pEM2)} \tag{2}$$

$$\mathrm{FEI}-2 = \frac{pEM4}{(pEM3 + pEM4)} \tag{3}$$

where pEMx indicates the proportion of EMx. A locally estimated scatterplot smoothing (LOESS) method is applied to the results of the two indexes to prevent undue emphasis being placed on single data points (Fig. 8c, d). From SU-1 to SU-2, FEI-1 decreases steadily while FEI-2 is consistently low. The decreasing FEI-1 conforms to the fining-upward trend (Fig. 3b). Both indexes increase quickly from SU-2 to SU-3. Within SU-3 only FEI-2 starts to reduce. In the upper three units, both the indexes maintain a relatively high value (~0.6) with fluctuations (Fig. 8c, d).

Fig. 9 shows the time series of the two indexes, the sedimentation rate, the AP/NAP values, the TOM and the calcium carbonate content based on the De Ham age model presented in Fig. 8. The variations of the two indexes are also compared with the NGRIP ice core $\delta^{18}O$ (Fig. 9b). Both indexes show higher flood conditions during the IACP than that in the Late Allerød, whereas the Greenland ice core $\delta^{18}O$ shows an anti-phase variation (Fig. 9b). At the Allerød-Younger Dryas transition, the Lower Meuse experienced quickly intensified flooding and a high sedimentation rate (Fig. 9b, c), and these hydrological changes co-varied with the rapidly declined $\delta^{18}O$ in Greenland ice core. During the IACP a temporary period of wet conditions at the Lower Meuse valley was also reported by Bohncke et al. (1993) and Hoek (1997). A simultaneous decline in winter temperature allowed for more intense freeze-thaw incidences which reduced soil infiltration capacity and, therefore, increased run-off and peak discharges during the spring time. This explanation also applies to the intensified floods at the start of Younger Dryas. The presence of initial ice-wedge casts and other periglacial features at the start of Younger Dryas point to the permafrost conditions and a mean annual temperature between −2 and −5 °C, and this could further induce more frequent and higher

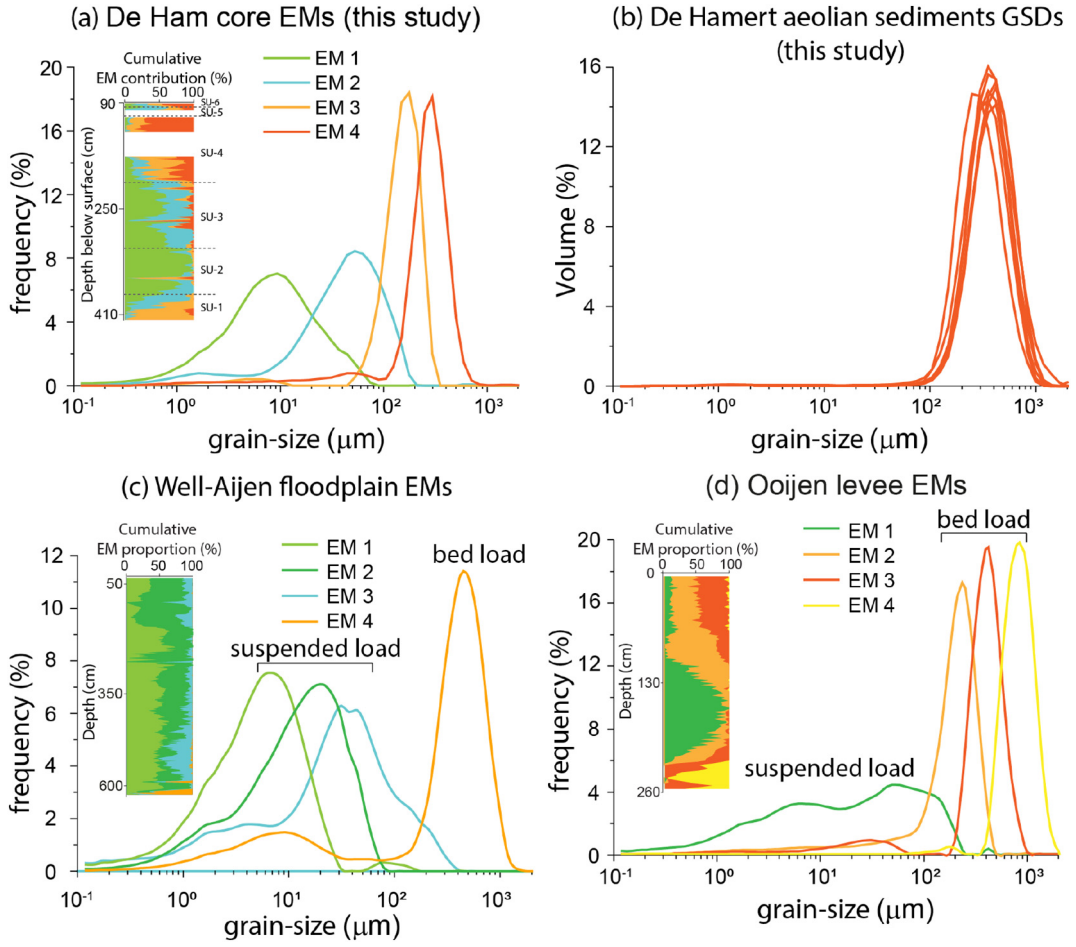

Fig. 10. The modelled end members from the De Ham site (this study) and from the Well-Aijen and Ooijen sites (after Peng et al., 2019 and Peng et al., 2020, respectively). End member modelling is not performed on the De Hamert aeolian sediment GSDs because of the small sample number and the uniform grain-size distributions.

floods. In the first stage of the Younger Dryas, both indexes show consistently high flooding conditions (Fig. 9b), whereas a discrepancy of the two indexes is observed in the second stage of the Younger Dryas (Fig. 9b), during which the consistently high floods indicated by FEI-1 index are not observed in the FEI-2 index. This disagreement can be explained by the influx of coarse aeolian sediments during the second phase of the Younger Dryas. The aeolian activity altered the dominant sediment source for the De Ham core and blurred the flooding signal stored in the fluvial bed load sediments. In addition, during this period, the Meuse continuously incised and migrated to the east (Fig. 1C) (Kasse et al., 1995). Therefore, the core site was less prone to be inundated by floods, which explains the higher FEI-1 but lower sedimentation rate in the second phase of Younger Dryas compared to the Allerød period.

The observations above have two main implications. Firstly, our results show that the Lower Meuse hydrological regime is very sensitive to the North Atlantic regional climate shifts during the last deglaciation. Secondly, it indicates that well-preserved Lateglacial flood-induced sediment records can be used to reconstruct past flooding stages by applying the end-member modelling approach. However, it should be stated that the obtained results following such an approach is highly dependent on the sedimentological setting of the studied sedimentary sequence. For example, in specific fluvial environments only background fine suspended load sediments (i.e., in distal floodplain environments with low energy floods) or coarse bed load components (i.e., at levee sites that receive high-energy deposition) are available for sampling, and the flooding indicators (such as sand layers, lithology changes, sedimentary texture and structure changes, interbedded palaeosols) can hardly be observed from the relatively homogenous deposits. Here, we show that the flooding stage signal is reflected by highlighting the coarse grained end members in the sediment fill of an abandoned channel, in accordance with the previous Holocene paleoflooding reconstructions (Peng et al., 2019; Peng et al., 2020), in which the flooding stages were reconstructed by analyzing the fine and coarse sediments from floodplain and levee environments, respectively.

6. Conclusions

The De Ham core from the Lower Meuse provides a well-preserved fluvial sediment record covering the Allerød up to the middle Holocene. The present study mainly focuses on the Allerød-Younger Dryas part of the record. The fine sediment characteristics, abundant aquatic plant and fauna taxa indicate a lake environment. Laboratory analyses provided AMS ^{14}C dating, grain size, oxygen and carbon isotopes of opercula biogenic carbonate, organic matter content, calcium carbonate content, pollen- and macrofossil-based vegetation and environmental reconstruction for the core.

In the Allerød, the sediments have a high organic matter content, sediments are fine-grained (clay) and accumulation rates are relatively high. The local landscape was characterized by high arboreal coverage. The macrofossil abundance reached their highest levels. The correlations between the calcium carbonate content and δ^{18}O and δ^{13}C variations indicate a high evaporation effect on carbonate chemistry of the lake environments during the Allerød period. Meanwhile, the intra-Allerød Cold Period is also recorded by the δ^{18}O of opercula biogenic

carbonate in the De Ham core. Sediments deposited in the Younger Dryas have lower organic matter and calcium carbonate content, and sediments gradually coarsen because of an increased influx of coarse silts and (partly aeolian) sands. Sedimentation rate is the highest in the first stage of the Younger Dryas. Compared to the preceding period, AP taxa are less prominent and pollen sum and number of macrofossil species are reduced. Subsequently, the appearance of Ericales and more upland herbs in the second stage of the Younger Dryas imply a more open landscape. The aeolian influx increased, likely as a result of strong westerlies and more open vegetation conditions.

Two flood energy indexes, FEI-1 and FEI-2, are constructed based on the grain size end members. FEI-1 uses the suspended load end-members, and FEI-2 is based on the bed load end-members. Both indexes show relatively high flood conditions during the IACP, followed by a low flood stage in the Late Allerød and quickly intensified flood conditions at the onset of the Younger Dryas. This study firstly revealed the high sensitivity of the local hydrological processes and sedimentary environments in the Lower Meuse catchment to the regional climate system. However, the flooding signal can be disturbed by other depositional processes such as aeolian input or local reworking. Therefore, we suggest the sediment source analysis should be justified prior to flooding reconstruction.

Declaration of competing interest

The authors declare that they have no known competing financial interests or personal relationships that could have appeared to influence the work reported in this paper.

Acknowledgments

M. van Leeuwen and other master students from VU Amsterdam collected preliminary sedimentary information for this study in the field and in the laboratory. We thank M. Hagen, S. Dijkman and S.J.A. Verdegaal for laboratory assistance. We thank the two anonymous reviewers for their constructive comments. This research was supported by a China Scholarship Council fellowship (201506410053) to F. Peng.

References

Bohncke, S., Vandenberghe, J.E.F., Coope, R., Reiling, R., 1987. Geomorphology and palaeoecology of the Mark valley (southern Netherlands): palaeoecology, palaeohydrology and climate during the Weichselian Late Glacial. Boreas 16 (1), 69–85. https://doi.org/10.1111/j.1502-3885.1987.tb00756.x.

Bohncke, S., Vandenberghe, J., Huijzer, A., 1993. Periglacial environments during the Weichselian Late Glacial in the Maas valley, the Netherlands. Netherlands Journal of Geosciences-Geologie en Mijnbouw 72, 193–210.

Bos, J.A.A., Zuidhoff, F.S., 2015. De restgeul van Well-Aijen. Een reconstructie van de vegetatieontwikkeling van het Noord-Limburgse Meusedal gedurende het Holoceen (Mesolithicum-Vroeg Romeinse tijd). ADC-rapport 3599, ADC ArcheoProjecten, the Netherlands.

Bos, J.A.A., van Geel, B., van der Plicht, J., Bohncke, S.J.P., 2007. Preboreal climate oscillations in Europe: Wiggle-match dating and synthesis of Dutch high-resolution multi-proxy records. Quat. Sci. Rev. 26 (15), 1927–1950. https://doi.org/10.1016/j.quascirev.2006.09.012.

Brauer, A., Endres, C., Günter, C., Litt, T., Stebich, M., Negendank, J.F.W., 1999. High resolution sediment and vegetation responses to Younger Dryas climate change in varved lake sediments from Meerfelder Maar, Germany. Quat. Sci. Rev. 18 (3), 321–329. https://doi.org/10.1016/S0277-3791(98)00084-5.

Brauer, A., Haug, G.H., Dulski, P., Sigman, D.M., Negendank, J.F.W., 2008. An abrupt wind shift in western Europe at the onset of the Younger Dryas cold period. Nat. Geosci. 1 (8), 520–523. https://doi.org/10.1038/ngeo263.

Clark, P.U., Shakun, J.D., Baker, P.A., Bartlein, P.J., Brewer, S., Brook, E., Carlson, A.E., Cheng, H., Kaufman, D.S., Liu, Z., Marchitto, T.M., Mix, A.C., Morrill, C., Otto-Bliesner, B.L., Pahnke, K., Russell, J.M., Whitlock, C., Adkins, J.F., Blois, J.L., Clark, J., Colman, S.M., Curry, W.B., Flower, B.P., He, F., Johnson, T.C., Lynch-Stieglitz, J., Markgraf, V., McManus, J., Mitrovica, J.X., Moreno, P.I., Williams, J.W., 2012. Global climate evolution during the last deglaciation. Proc. Natl. Acad. Sci. 109 (19), E1134. https://doi.org/10.1073/pnas.1116619109.

De Mulder, F.J., Geluk, M.C., Ritsema, I., Westerhoff, W.E., Wong, T.E., 2003. De ondergrond van Nederland. Wolters-Noordhof, Groningen, p. 379.

Erkens, G., Toonen, W.H.J., Cohen, K.M., Prins, M.A., 2013. Unravelling mixed sediment signals in the floodplains of the Rhine catchment using end member modelling of grain size distributions. 10th International Conference on Fluvial Sedimentology. University of Leeds, pp. 109–110.

Faegri, K., Kaland, P.E., Iversen, J., 1989. Textbook of Pollen Analysis. John Wiley & Sons, Ltd, p. 328.

Fretter, V., Graham, A., 1976. The Prosobranch Molluscs of Britain and Denmark, Part 2 (Angus Graham Associates).

Gaillard, M.J., Birks, H.H., 2007. Plant macrofossil methods and studies | paleolimnological applications. In: Elias, S.A. (Ed.), Encyclopedia of Quaternary Science. Elsevier, Oxford, pp. 2337–2356.

Gittenberger, E., Janssen, A.W., Kuijper, W., Kuiper, J., Meijer, T., Van der Velde, G., De Vries, J., 2004. De Nederlandse Zoetwatermollusken: Recente en fossiele weekdieren uit zoet en brak water (Nationaal Natuurhistorisch Museum Naturalis).

Graham, A., 1988. Molluscs: Prosobranchs and Pyramidellid Gastropods: Keys and Notes for the Identification of the Species, 2 (Brill Archive).

Grimm, E., 1992. TILIA and TILIA-GRAPH: Pollen Spreadsheet and Graphics Programs, 8th International Palynological Congress (Aix-en-Provence).

Grimm, E., 2004. TGView Version 2.0. 2. Illinois State Museum, Springfield.

Heiri, O., Lotter, A.F., Lemcke, G., 2001. Loss on ignition as a method for estimating organic and carbonate content in sediments: reproducibility and comparability of results. J. Paleolimnol. 25 (1), 101–110. https://doi.org/10.1023/A:1008119611481.

Hepp, J., Wüthrich, L., Bromm, T., Bliedtner, M., Schäfer, I.K., Glaser, B., Rozanski, K., Sirocko, F., Zech, R., Zech, M., 2019. How dry was the Younger Dryas? Evidence from a coupled δ2H–δ18O biomarker paleohygrometer applied to the Gemündener Maar sediments, Western Eifel. Germany. Clim. Past 15 (2), 713–733. https://doi.org/10.5194/cp-15-713-2019.

Hoek, W.Z., 1997. Late-glacial and early Holocene climatic events and chronology of vegetation development in the Netherlands. Veg. Hist. Archaeobotany 6 (4), 197–213. https://doi.org/10.1007/BF01370442.

Hoek, W.Z., Bohncke, S.J.P., 2002. Climatic and environmental events over the Last Termination, as recorded in The Netherlands: a review. Netherlands Journal of Geosciences - Geologie en Mijnbouw 81 (1), 123–137. https://doi.org/10.1017/S001677460002062X.

Hoek, W.Z., Lammertsma, E.I., Bohncke, S.J.P., Bos, J.A.A., Bunnik, F., Kasse, C., Schokker, J., Westerhoff, W., 2017. Lateglacial and early Holocene vegetation development and fluvial system changes in the northern Meuse valley, the Netherlands: a review of palynological data. Neth. J. Geosci. 96 (2), 93–114. https://doi.org/10.1017/njg.2017.4.

Huisink, M., 1997. Late-glacial sedimentological and morphological changes in a lowland river in response to climatic change: the Maas, southern Netherlands. J. Quat. Sci. 12 (3), 209–223. https://doi.org/10.1002/(SICI)1099-1417(199705/06)12:3<209::AID-JQS306>3.0.CO;2-P.

Isarin, R.F.B., Bohncke, S.J.P., 1999. Mean July temperatures during the Younger Dryas in northwestern and central Europe as inferred from climate indicator plant species. Quat. Res. 51 (2), 158–173. https://doi.org/10.1006/qres.1998.2023.

Isarin, R.F.B., Renssen, H., Vandenberghe, J., 1998. The impact of the North Atlantic Ocean on the Younger Dryas climate in northwestern and central Europe. J. Quat. Sci. 13 (5), 447–453. https://doi.org/10.1002/(SICI)1099-1417(1998090)13:5<447::AID-JQS402>3.0.CO;2-B.

Iversen, J., 1973. The development of Denmark's nature since the last glacial. Geology of Denmark. 3. C.A. Reitzels Forlag, København.

Kasse, C., 2002. Sandy aeolian deposits and environments and their relation to climate during the Last Glacial Maximum and Lateglacial in northwest and central Europe. Progress in Physical Geography: Earth and Environment 26 (4), 507–532. https://doi.org/10.1191/0309133302pp350ra.

Kasse, C., Vandenberghe, J., Bohncke, S.J.P., 1995. Climatic change and fluvial dynamics of the Maas during the Late Weichselian and Early Holocene. In: Vandenberghe, C., Kasse, S.J.P., Bohncke, G.B. (Eds.), F. B., J. European river activity and climatic change during the Lateglacial and early Holocene, Paläoklimaforschung, pp. 123–150.

Kolstrup, E., 2007. Lateglacial older and younger coversand in northwest Europe: chronology and relation to climate and vegetation. Boreas 36 (1), 65–75. https://doi.org/10.1111/j.1502-3885.2007.tb01181.x.

Konert, M., Vandenberghe, J.E.F., 1997. Comparison of laser grain size analysis with pipette and sieve analysis: a solution for the underestimation of the clay fraction. Sedimentology 44 (3), 523–535. https://doi.org/10.1046/j.1365-3091.1997.d01-38.x.

Leng, M.J., Marshall, J.D., 2004. Palaeoclimate interpretation of stable isotope data from lake sediment archives. Quat. Sci. Rev. 23 (7), 811–831. https://doi.org/10.1016/j.quascirev.2003.06.012.

Leng, M., Roberts, N., Reed, J., Sloane, H., 1999. Late Quaternary climatic and limnological variations based on carbon and oxygen isotope data from authigenic and ostracod carbonate in the Konya Basin, Turkey. J. Paleolimnol. 22, 187–204.

Meyers, P.A., Teranes, J.L., 2002. Sediment organic matter, Tracking environmental change using lake sediments. Springer, pp. 239–269.

Moore, P.D., Webb, J.A., Collison, M.E., 1991. Pollen Analysis. Blackwell scientific publications.

Muschitiello, F., Pausata, F.S.R., Watson, J.E., Smittenberg, R.H., Salih, A.A.M., Brooks, S.J., Whitehouse, N.J., Karlatou-Charalampopoulou, A., Wohlfarth, B., 2015. Fennoscandian freshwater control on Greenland hydroclimate shifts at the onset of the Younger Dryas. Nat. Commun. 6 (1), 8939. https://doi.org/10.1038/ncomms9939.

Paterson, G.A., Heslop, D., 2015. New methods for unmixing sediment grain size data. Geochem. Geophys. Geosyst. 16 (12), 4494–4506. https://doi.org/10.1002/2015GC006070.

Peng, F., Prins, M.A., Kasse, C., Cohen, K.M., Van der Putten, N., van der Lubbe, J., Toonen, W.H.J., van Balen, R.T., 2019. An improved method for paleoflood reconstruction and flooding phase identification, applied to the Meuse River in the Netherlands. Glob. Planet. Chang. 177, 213–224. https://doi.org/10.1016/j.gloplacha.2019.04.006.

Peng, F., Kasse, C., Prins, M.A., Ellenkamp, R., Krasnoperov, M.Y., van Balen, R.T., 2020. Paleoflooding reconstruction from Holocene levee deposits in the lower Meuse

valley, the Netherlands. Geomorphology 352, 107002. https://doi.org/10.1016/j.geomorph.2019.107002.
Prins, M.A., 1999. Pelagic, hemipelagic and turbidite deposition in the Arabian Sea during the late Quaternary: unravelling the signals of eolian and fluvial sediment supply as functions of tectonics, sea-level and climatic change by means of end-member modelling of siliciclastic grain-size distributionsPhD Thesis, Universiteit Utrecht, the Netherlands.
Prins, M.A., Weltje, G.J., 1999. End-member modeling of siliciclastic grain-size distributions: The late Quaternary record of aeolian and fluvial sediment supply to the Arabian Sea and its paleoclimatic significance. In: J. Harbaugh (Ed.), Numerical experiments in stratigraphy: Recent advances in stratigraphic and sedimentologic computer simulations. Society for Sedimentary Geology, pp. 91–111.
Prins, M.A., Vriend, M., Nugteren, G., Vandenberghe, J., Lu, H., Zheng, H., Jan Weltje, G., 2007. Late Quaternary aeolian dust input variability on the Chinese Loess Plateau: inferences from unmixing of loess grain-size records. Quat. Sci. Rev. 26 (1), 230–242. https://doi.org/10.1016/j.quascirev.2006.07.002.
Rasmussen, S.O., Andersen, K.K., Svensson, A.M., Steffensen, J.P., Vinther, B.M., Clausen, H.B., Siggaard-Andersen, M.-L., Johnsen, S.J., Larsen, L.B., Dahl-Jensen, D., Bigler, M., Röthlisberger, R., Fischer, H., Goto-Azuma, K., Hansson, M.E., Ruth, U., 2006. A new Greenland ice core chronology for the last glacial termination. Journal of Geophysical Research: Atmospheres 111 (D6). https://doi.org/10.1029/2005jd006079.
Rasmussen, S.O., Bigler, M., Blockley, S.P., Blunier, T., Buchardt, S.L., Clausen, H.B., Cvijanovic, I., Dahl-Jensen, D., Johnsen, S.J., Fischer, H., Gkinis, V., Guillevic, M., Hoek, W.Z., Lowe, J.J., Pedro, J.B., Popp, T., Seierstad, I.K., Steffensen, J.P., Svensson, A.M., Vallelonga, P., Vinther, B.M., Walker, M.J.C., Wheatley, J.J., Winstrup, M., 2014. A stratigraphic framework for abrupt climatic changes during the Last Glacial period based on three synchronized Greenland ice-core records: refining and extending the INTIMATE event stratigraphy. Quat. Sci. Rev. 106, 14–28. https://doi.org/10.1016/j.quascirev.2014.09.007.
Reimer, P.J., Bard, E., Bayliss, A., Beck, J.W., Blackwell, P.G., Ramsey, C.B., Buck, C.E., Cheng, H., Edwards, R.L., Friedrich, M., Grootes, P.M., Guilderson, T.P., Haflidason, H., Hajdas, I., Hatté, C., Heaton, T.J., Hoffmann, D.L., Hogg, A.G., Hughen, K.A., Kaiser, K.F., Kromer, B., Manning, S.W., Niu, M., Reimer, R.W., Richards, D.A., Scott, E.M., Southon, J.R., Staff, R.A, Turney, C.S.M., van der Plicht, J., 2013. IntCal13 and Marine13 radiocarbon age calibration curves 0–50,000 years cal BP. Radiocarbon 55 (4), 1869–1887. https://doi.org/10.2458/azu_js_rc.55.16947.
Renssen, H., Lautenschlager, M., Schuurmans, C.J.E., 1996. The atmospheric winter circulation during the Younger Dryas stadial in the Atlantic/European sector. Clim. Dyn. 12 (12), 813–824. https://doi.org/10.1007/s003820050145.
Roberts, N., Jones, M.D., Benkaddour, A., Eastwood, W.J., Filippi, M.L., Frogley, M.R., Lamb, H.F., Leng, M.J., Reed, J.M., Stein, M., Stevens, L., Valero-Garcés, B., Zanchetta, G., 2008. Stable isotope records of Late Quaternary climate and hydrology from Mediterranean lakes: the ISOMED synthesis. Quat. Sci. Rev. 27 (25), 2426–2441. https://doi.org/10.1016/j.quascirev.2008.09.005.
Schenk, F., Väliranta, M., Muschitiello, F., Tarasov, L., Heikkilä, M., Björck, S., Brandefelt, J., Johansson, A.V., Näslund, J.-O., Wohlfarth, B., 2018. Warm summers during the Younger Dryas cold reversal. Nat. Commun. 9 (1), 1634. https://doi.org/10.1038/s41467-018-04071-5.
Schoffelmeer, C., 2014. On the response of the river Meuse to Late Glacial climate change in the lower Meuse valley. Master Thesis, Vrije Universiteit Amsterdam.
Streeter, D., Hart-Davies, C., Hardcastle, A., Harper, L., Cole, F., 2016. Collins Wild Flower Guide. HarperCollins Publishers Limited.
Stuiver, M., 1970. Oxygen and carbon isotope ratios of fresh-water carbonates as climatic indicators. Journal of Geophysical Research (1896–1977) 75 (27), 5247–5257. https://doi.org/10.1029/JC075i027p05247.
Stuiver, M., Grootes, P.M., 2000. GISP2 oxygen isotope ratios. Quat. Res. 53 (3), 277–284. https://doi.org/10.1006/qres.2000.2127.
Stuut, J.-B.W., Prins, M.A., Schneider, R.R., Weltje, G.J., Jansen, J.H.F., Postma, G., 2002. A 300-kyr record of aridity and wind strength in southwestern Africa: inferences from grain-size distributions of sediments on Walvis Ridge, SE Atlantic. Mar. Geol. 180 (1), 221–233. https://doi.org/10.1016/S0025-3227(01)00215-8.
Tebbens, L.A., Veldkamp, A., Westerhoff, W., Kroonenberg, S.B., 1999. Fluvial incision and channel downcutting as a response to Late-glacial and Early Holocene climate change: the lower reach of the River Meuse (Maas), The Netherlands. J. Quat. Sci. 14 (1), 59–75. https://doi.org/10.1002/(SICI)1099-1417(199902)14:1%3C59::AID-JQS408%3E3.0.CO;2-Z.
Teranes, J.L., McKenzie, J.A., 2001. Lacustrine oxygen isotope record of 20th-century climate change in central EuropeL evaluation of climatic controls on oxygen isotopes in precipitation. J. Paleolimnol. 26 (2), 131–146. https://doi.org/10.1023/A:1011175701502.
Teunissen, D., 1983. The development of the landscape of the nature reserve De Hamert and its environs in the Northern part of the province of Limburg, The Netherlands. Geol. Mijnb. 62 (4), 8.
Toonen, W.H.J., Winkels, T.G., Cohen, K.M., Prins, M.A., Middelkoop, H., 2015. Lower Rhine historical flood magnitudes of the last 450 years reproduced from grain-size measurements of flood deposits using End Member Modelling. CATENA 130, 69–81. https://doi.org/10.1016/j.catena.2014.12.004.
Van Geel, B., Coope, G.R., Van Der Hammen, T., 1989. Palaeoecology and stratigraphy of the lateglacial type section at Usselo (the Netherlands). Rev. Palaeobot. Palynol. 60 (1), 25–129. https://doi.org/10.1016/0034-6667(89)90072-9.
Van Hateren, J.A., Prins, M.A., van Balen, R.T., 2018. On the genetically meaningful decomposition of grain-size distributions: a comparison of different end-member modelling algorithms. Sediment. Geol. 375, 49–71. https://doi.org/10.1016/j.sedgeo.2017.12.003.
Van Huissteden, J., Kasse, C., 2001. Detection of rapid climate change in Last Glacial fluvial successions in The Netherlands. Glob. Planet. Chang. 28 (1), 319–339. https://doi.org/10.1016/S0921-8181(00)00082-5.
Van Leeuwen, M., 2014. Response of the Maas River to Climatic Changes of the Late Pleniglacial to Holocene Master Thesis. Vrije Universiteit Amsterdam (73 pp.).
Vandenberghe, J., Kasse, C., Bohncke, S., Kozarski, S., 1994. Climate-related river activity at the Weichselian-Holocene transition: a comparative study of the Warta and Maas rivers. Terra Nova 6 (5), 476–485. https://doi.org/10.1111/j.1365-3121.1994.tb00891.x.
Weltje, G.J., 1997. End-member modeling of compositional data: Numerical-statistical algorithms for solving the explicit mixing problem. Math. Geol. 29 (4), 503–549. https://doi.org/10.1007/BF02775085.
Wentworth, C.K., 1922. A scale of grade and class terms for clastic sediments. The Journal of Geology 30 (5), 377–392. https://doi.org/10.1086/622910.
Woolderink, H., Kasse, C., Cohen, K.M., Hoek, W.Z., Van Balen, R., 2018. Spatial and temporal variations in river terrace formation, preservation, and morphology in the Lower Meuse Valley. The Netherlands. Quaternary Research, 1–22 https://doi.org/10.1017/qua.2018.49.